JOURNAL OF THERMOPHYSICS AND HEAT TRANSFER
Vol. 13, No. 1, January–March 1999

Calculation of Radiating Flowfield Behind a Reflected Shock Wave in Air

Takeharu Sakai,* Keisuke Sawada,† and Chul Park‡
Tohoku University, Sendai 980-8579, Japan

A numerical method is developed for calculating a one-dimensional radiating flowfield in thermochemical equilibrium in which radiation strongly affects the flowfield. Radiative heat fluxes are calculated using a model developed earlier that combines Planck, Rosseland, and gray-gas models. The flow solution is obtained with a fully implicit time-marching method using a full-block matrix inversion. The method is used to determine the radiating flowfield behind a reflected shock wave in air. It is shown that the method converges at enthalpies up to 100 MJ/kg and pressure up to 5 atm, and that the calculated radiative heat flux values agree fairly well with the experimental data taken at enthalpies of up to 80 MJ/kg.

Nomenclature

B_λ = blackbody (Planck) function at given wavelength λ, W/(cm^2-sr-μm)
E_n = exponential integral function of order n
e = total energy, J/m^3
I_λ = radiation intensity at given wavelength λ, W/(cm^2-sr-μm)
l = directional cosine
p = pressure, N/m^2 or atm
q = radiative heat flux, W/cm^2
T = temperature, K
t = time, s
u = velocity, m/s
V = incident shock velocity, km/s
x = distance from an upstream reference point, m
$\Delta\tau_P$, $\Delta\tau_R$ = selection criteria of the Planck–Rosseland–Gray model
κ_λ = absorption coefficient at given wavelength including stimulated emission, cm^{-1}
ρ = density, kg/m^3
τ = optical depth measured from an upstream reference point

Subscripts

G = gray-gas mean
P = Planck mean
R = Rosseland mean
w = wall
λ = wavelength, μm
0 = upstream reference point

Superscripts

$+$ = direction from an upstream reference point to the wall
$-$ = direction from the wall to an upstream reference point

Introduction

A SPACE vehicle entering a planetary atmosphere at a hypersonic speed is subject to significant radiative heating. The radiation from a high-temperature gas behind a shock wave affects the flowfield properties, which in turn affect radiative properties. Such a strong radiating flowfield is believed to have occurred in the flights of the Fire vehicles, which entered into Earth's atmosphere at a velocity of 11.4 km/s[1]; the Pioneer–Venus Probes, which entered into Venusian atmosphere at a velocity of 11.5 km/s[2]; and the Galileo Probe, which entered into the Jovian atmosphere at a velocity of 45 km/s.[3] Similar strong radiating flowfields will be produced in future planetary missions such as MUSES-C, Stardust, and manned Mars missions that will enter the Earth's atmosphere at velocities of 12–16 km/s. In such situations, the flowfield must be calculated accounting for radiative transport.

To calculate the radiation in these entry environments accurately, a large number of wavelength points must be used because the absorption coefficient of the gas strongly depends on wavelength. Moreover, the radiation calculation must be repeated many times at every point in the flowfield. Although a line-by-line method such as NEQAIR[4] can calculate radiation phenomena in detail, it is not suited for the coupled calculation with the flowfield because the computing time becomes prohibitively large. Recently, a multiband model has been developed to reduce the computing time of the line-by-line method.[5,6] The multiband model has successfully reduced the computing time at least by a factor of 100. This model can reproduce a line-by-line calculation within a small error.[5,6]

Radiative heat flux at a point is a function of all conserved variables at all points in the flowfield. The resulting set of conservation equations is a system of nonlinear integro-differential equations. To solve this system, two methods of calculation were used. One is the loosely coupled method, which works well when radiation is weak. Another is the fully coupled method, which is used when radiation is strong. In the loosely coupled calculation, the following steps are needed: 1) flow solution is first obtained without radiation, 2) radiation is calculated from this flow solution, and 3) the flowfield calculation accounting for this radiation is carried out once for a certain number of iterations with the fixed radiative source term. Steps 2 and 3 are repeated until the converged solution is obtained. In the fully coupled calculation, on the other hand, both the flowfield and the radiation are updated for every iteration.

Received Dec. 1, 1997; presented as Paper 98-0861 at the AIAA 36th Aerospace Sciences Meeting, Reno, NV, Jan. 12–15, 1998; revision received Aug. 19, 1998; accepted for publication Aug. 21, 1998.

*Graduate Student, Department of Aeronautics and Space Engineering. Student Member AIAA.

†Professor, Department of Aeronautics and Space Engineering. Senior Member AIAA.

‡Professor, Department of Aeronautics and Space Engineering; currently Staff Scientist, NASA Ames Research Center, Thermosciences Institute, M/S 230-2, Moffett Field, CA 94035. Associate Member AIAA.

Loosely coupled calculations have been carried out to calculate the radiating flowfield for Lunar and Mars return conditions,[7] or to reproduce the Fire II flight data.[8] In these loosely coupled calculations, the radiation was treated explicitly using the multiband model. A fully coupled calculation has been made to determine the radiating flowfield for the Fire II flight condition[9] and the Galileo flight condition,[10] or to calculate quasi-one-dimensional flowfield.[5,11] The computational equations that appeared in Ref. 9 were solved using an iteration technique such as the Gauss–Seidel method. In the calculation of the flowfield of Galileo Probe, the viscous shock-layer method was used.[10] The solution of the entire flowfield was obtained by a space-marching technique from the stagnation region to the downstream region. In Refs. 5 and 11, the computational equations were solved using the full-block matrix inversion. For both of these calculations, converged solutions were obtained. Radiation calculations appearing in the previously mentioned references are carried out assuming a tangent slab approximation.

There are two limitations in the past radiation-coupled[5,7–9,11] computational fluid dynamics (CFD) calculations. First, the past works showed that the highest flight velocity and stagnation pressure calculated were only 16 km/s and the order of 10^{-1} atm for a one-dimensional flowfield,[12] and 13.6 km/s and the order of 10^{-2} atm for a two-dimensional flowfield.[7] As the flow enthalpy and pressure increase, the interactions between radiation and flow motion become more intense. For future missions of interest, solutions at higher flow velocities are needed.

The second limitation is on the required computing time. Radiation calculations have been made assuming that radiation occurs only across the shock layer, thereby limiting the radiation calculation to one dimension. For the fully coupled calculation, the computing time for such one-dimensional calculation is at the limit of practicability using the multiband model.[5,11] For a realistic calculation, a two-dimensional calculation will be necessary. Two-dimensional fully coupled calculations that do not resort to the tangent slab approximation are impractical with the multiband model.

A theoretical model named the Planck–Rosseland–Gray (PRG) model has been developed for the purpose of reducing computing time for radiative transport calculations.[13] The PRG model calculates radiative heat fluxes using three mean absorption coefficients, i.e., Planck, Rosseland, and gray-gas. This model can closely reproduce the radiative heat flux values obtained by a detailed line-by-line calculation.[13] The model has reduced the computing time of the multiband model at least by a factor of 10.

The purpose of the present work is to develop a fully coupled method using the PRG model. Unlike other radiation models, the characteristic mean values are problem specific and, therefore, it is not intuitively clear that a well-converging fully coupled method can be constructed with the PRG model. The method is applied here for a one-dimensional problem, with the intention of applying it for a two-dimensional problem in the future.

The main effort is expended in the present work to develop a scheme that converges at an enthalpy equivalent to a flight speed of 16 km/s, which is anticipated for future missions. Pressure values greater than 1 atm are also targeted. The present method is validated against an existing set of experimental data. In the 1960s, the radiant intensity of high-temperature air was measured in a shock tube.[14] The shock velocity range of 6.5–9.4 km/s was attained in the experiment. This velocity range corresponds to a flight speed range of 9.5–14 km/s at an altitude of 43 km.[14] These conditions are evaluated by the density value calculated through a hypersonic approximate relation[15] for a strong normal shock wave using the pressure and enthalpy values in the postreflected shock region. At the lower shock velocity range of 6.5–7.5 km/s, a good agreement between the calculations and the experiments was obtained.[14] At a higher shock velocity range of 7.5–9 km/s, however, a discrepancy of a factor of up to 2 was seen.[14] Possible reasons for this disagreement are given in this paper.

Method of Calculation

Radiative Heat Flux

The total radiative heat flux q is calculated using the PRG model.[13] Although the derivation of the PRG model is given in Ref. 13, a brief review is made here for completeness. The intensity of radiation at a given λ, I_λ, satisfies the radiative transfer equation

$$l\frac{\partial I_\lambda}{\partial x} = \kappa_\lambda (B_\lambda - I_\lambda) \tag{1}$$

q is given by integrating $I_\lambda \times l$ over solid angle $d\Omega$ and wavelength

$$\begin{aligned} q &= \iint I_\lambda \, l \, d\Omega \, d\lambda \\ &= \int_{\theta=0}^{2\pi}\int_{\phi=0}^{\pi} Il \sin\phi \, d\phi \, d\theta \\ &= 2\pi \int_{-1}^{1} Il \, dl \end{aligned} \tag{2}$$

where

$$I \equiv \int I_\lambda \, d\lambda$$

The total radiative heat flux is given by

$$q = q_{\text{PRG}}^{+} + q_{\text{PRG}}^{-} \tag{3}$$

where

$$\begin{aligned} q_{\text{PRG}}^{+} &= 2\pi \int_0^1 (I_P + I_R + I_G) l \, dl \\ &= q_P^+ + q_R^+ + q_G^+ \\ q_{\text{PRG}}^{-} &= 2\pi \int_{-1}^0 (I_P + I_R + I_G) l \, dl \\ &= q_P^- + q_R^- + q_G^- \end{aligned}$$

Here

$$q_P^+ = 2\pi\left(\frac{1}{2} I_{0_P} + \int_0^x \kappa_P B_P \, d\hat{x}\right) \tag{4}$$

$$q_P^- = -2\pi\left(\frac{1}{2} I_{w_P} + \int_x^{x_w} \kappa_P B_P \, d\hat{x}\right) \tag{5}$$

$$q_R^+ = \pi B_R - \frac{2}{3}\pi \frac{\left(\dfrac{dB}{dT}\right)_R}{\kappa_R}\frac{dT}{dx} \tag{6}$$

$$q_R^- = -\pi B_R - \frac{2}{3}\pi \frac{\left(\dfrac{dB}{dT}\right)_R}{\kappa_R}\frac{dT}{dx} \tag{7}$$

$$q_G^+ = 2\pi \int_0^x \kappa_G B_G E_2[\tau(x) - \tau(\hat{x})] \, d\hat{x} + 2\pi I_{0_G} E_3[\tau(x)] \tag{8}$$

$$q_G^- = -2\pi \int_x^{x_w} \kappa_G B_G E_2[\tau(\hat{x}) - \tau(x)] \, d\hat{x} + 2\pi I_{w_G} E_3[\tau(x_w) - \tau(x)] \tag{9}$$

where

$$\tau(x) = \int_0^x \kappa \, \mathrm{d}x$$

$$E_n(z) = \int_0^1 l^{n-2} \exp\left(-\frac{z}{l}\right) \mathrm{d}l$$

$$E_n'(z) = -E_{n-1}(z), \qquad n > 1$$

By taking the flow properties to be constant within each cell and by denoting the quantity $E_n[\tau(x) - \tau(\hat{x})]$ as $E_n(j, \hat{j})$, the computational equations for Eqs. (4–9) are given, respectively, as

$$q^+_{P_j} = 2\pi[\tfrac{1}{2}I_{0_P} + \kappa_{P_1}B_{P_1}\Delta x_1 + \kappa_{P_2}B_{P_2}\Delta x_2 + \cdots + \kappa_{P_j}B_{P_j}(\Delta x_j/2)] \tag{10}$$

$$q^-_{P_j} = -2\pi[\tfrac{1}{2}I_{w_P} + \kappa_{P_j}B_{P_j}(\Delta x_j/2) + \kappa_{P_{j+1}}B_{P_{j+1}}\Delta x_{j+1} + \cdots + \kappa_{P_{j_\mathrm{max}}}B_{P_{j_\mathrm{max}}}\Delta x_{j_\mathrm{max}}] \tag{11}$$

$$q^+_{R_j} = \pi B_{R_j} - \frac{2}{3}\pi\frac{1}{\kappa_{R_j}}\frac{\mathrm{d}B_{R_j}}{\mathrm{d}T_j}\left(\frac{\mathrm{d}T}{\mathrm{d}x}\right)_j \tag{12}$$

$$q^-_{R_j} = -\pi B_{R_j} - \frac{2}{3}\pi\frac{1}{\kappa_{R_j}}\frac{\mathrm{d}B_{R_j}}{\mathrm{d}T_j}\left(\frac{\mathrm{d}T}{\mathrm{d}x}\right)_j \tag{13}$$

$$q^+_{G_j} = 2\pi[I_{0_G}E_3(j, 1) + \kappa_{G_1}B_{G_1}E_2(j, 1)\Delta x_1 + \kappa_{G_2}B_{G_2}E_2(j, 2)\Delta x_2 + \cdots + \kappa_{G_j}B_{G_j}E_2(j, j)(\Delta x_j/2)] \tag{14}$$

$$q^-_{G_j} = -2\pi[I_{w_G}E_3(j_\mathrm{max}, j) + \kappa_{G_j}B_{G_j}E_2(j, j)(\Delta x_j/2) + \kappa_{G_{j+1}}B_{G_{j+1}}E_2(j+1, j)\Delta x_{j+1} + \cdots + \kappa_{G_{j_\mathrm{max}}}B_{G_{j_\mathrm{max}}}E_2(j_\mathrm{max}, j)\Delta x_{j_\mathrm{max}}] \tag{15}$$

The exponential integral function E_n is evaluated by a polynomial expression given in Ref. 16. In the present study, I_0 is zero and I_w is the blackbody at the wall temperature. The wall is assumed to be at 3000 K. The value of I_w is given in the Planck mean part.

The absorption coefficients are evaluated first by a 2294 multiband model. In this model, the absorption coefficient is given as[5]

$$\kappa_\lambda = \exp(A_1/z + A_2 + A_3 \ell n\, z + A_4 z + A_5 z^2) \tag{16}$$

where $z = 10{,}000/T$. The A_1–A_5 values are the curve-fit parameters. Two different sets of fitting parameters are used for covering the different temperature ranges. One provides absorption coefficients in the temperature range of 6000–16,000 K, and another in 10,000–20,000 K.

In the PRG model, the radiative behavior at a given wavelength is classified into one of the three groups, that is, Planck, Rosseland, or gray-gas by the following rule[13]:

if $\Delta\tau_\lambda = \kappa_\lambda \Delta x < \Delta\tau_P$ then Planck approximation
if $\Delta\tau_\lambda > \Delta\tau_R$ then Rosseland approximation
otherwise then gray-gas approximation

where $\Delta\tau_P$ and $\Delta\tau_R$ are the selection criteria that are determined by an iteration method.[13] The value of $\Delta\tau_R$ is fixed for all calculated cases in this study. The iteration is repeated until the difference between the spatial heat flux distribution of the present method and that of the multiband model becomes about 1%. Although the typical convergence is obtained by the 30th iteration, the iteration is continued up to 50 times. These criteria provide the quantities denoted by the subscripts P, R, and G used in Eqs. (10–15). In the present PRG model, the gray-gas absorption coefficient is evaluated by the Rosseland mean absorption coefficient calculated within the gray-gas group. This differs from the previous method in which a combined formula of the Planck and the Rosseland mean absorption coefficients was employed as the gray-gas absorption coefficient.[13] The PRG model is constructed for both directions, i.e., from the shock wave to the wall and from the wall to the shock wave.

The input parameters required for the PRG model such as κ_P and B_P, etc., are a function of pressure, temperature, and the selection criteria $\Delta\tau_R$ and $\Delta\tau_P$. These parameters are interpolated by a bilinear interpolation from the nearby points in a prepared table. Two sets of tables were used corresponding to the two different sets of coefficients used in the multiband model mentioned earlier. One set covers the pressure range of 0.1–10 atm, and the temperature range of 6000–16,000 K. The second set covers temperatures from 10,000–20,000 K for the same pressure range. The tables provided the needed quantities at six pressure values, 21 temperature values, and 48 selection criteria values. For pressure and selection criteria values, logarithmic interpolations were used, whereas a linear interpolation was used for temperature.

Numerical Method

The conservation equations governing the flowfield can be written as

$$\frac{\partial Q}{\partial t} + \frac{\partial \boldsymbol{F}}{\partial x} = \frac{\partial \boldsymbol{F}_\mathrm{rad}}{\partial x} \tag{17}$$

where Q is the conserved variables, $\boldsymbol{F}$ is the convective flux vector, and $\boldsymbol{F}_\mathrm{rad}$ is the radiative heat flux vector. They are

$$Q = \begin{bmatrix} \rho \\ \rho u \\ e \end{bmatrix}, \qquad \boldsymbol{F} = \begin{bmatrix} \rho u \\ \rho u^2 + p \\ (e + p)u \end{bmatrix}, \qquad \boldsymbol{F}_\mathrm{rad} = \begin{bmatrix} 0 \\ 0 \\ -q \end{bmatrix} \tag{18}$$

A finite volume method is applied for discretizing Eq. (17). The implicit form of Eq. (17) becomes

$$\frac{\Delta Q}{\Delta t} + \frac{1}{\Delta x}(F^{n+1}_{i+1/2} - F^{n+1}_{i-1/2}) = \frac{1}{\Delta x}(F^{n+1}_{\mathrm{rad}_{i+1/2}} - F^{n+1}_{\mathrm{rad}_{i-1/2}}) \tag{19}$$

The Taylor series expansion of $F^{n+1}_{i+1/2}$ about time level n provides the relation

$$F^{n+1}_{i+1/2} = F^n_{i+1/2} + A^n_{i+1/2}\Delta Q_{i+1/2} \tag{20}$$

where A denotes the flux Jacobian $A = \partial F/\partial Q$. In this study, the numerical flux function $F^n_{i+1/2}$ is evaluated using the Steger–Warming flux vector splitting scheme,[17] and is given by

$$F^n_{i+1/2} = F^+_i + F^-_{i+1} \tag{21}$$

The $A^n_{i+1/2}\Delta Q_{i+1/2}$ is calculated using the flux vector splitting technique as follows:

$$A^n_{i+1/2}\Delta Q_{i+1/2} = A^{+n}_i \Delta Q_i + A^{-n}_{i+1}\Delta Q_{i+1} \tag{22}$$

In the previous equations, ± signs are a result of the sign of eigenvalues of the flux Jacobian. The MUSCL approach was used to improve spatial accuracy.

Radiative heat flux q is a function of all conserved variables at all spatial points, i.e.,

$$F^{n+1}_{\text{rad}_{i+1/2}} = F^{n}_{\text{rad}_{i+1/2}} + \sum_{j=1}^{i_{\max}} \frac{\partial F^{n}_{\text{rad}_{i+1/2}}}{\partial Q_{j+1/2}} \Delta Q_{j+1/2} \tag{23}$$

where

$$F^{n}_{\text{rad}_{i+1/2}} = \tfrac{1}{2}(F^{n}_{\text{rad}_i} + F^{n}_{\text{rad}_{i+1}}) \tag{24}$$

$$\sum_{j=1}^{i_{\max}} \frac{\partial F^{n}_{\text{rad}_{i+1/2}}}{\partial Q_{j+1/2}} \Delta Q_{j+1/2} = \frac{1}{2}\left(\sum_{j=1}^{i} \frac{\partial F^{n}_{\text{rad}_i}}{\partial Q_j} \Delta Q_j + \sum_{j=1}^{i_{\max}} \frac{\partial F^{n-}_{\text{rad}_i}}{\partial Q_j} \Delta Q_j + \sum_{j=1}^{i+1} \frac{\partial F^{n+}_{\text{rad}_{i+1}}}{\partial Q_j} \Delta Q_j + \sum_{j=i+1}^{i_{\max}} \frac{\partial F^{n-}_{\text{rad}_{i+1}}}{\partial Q_j} \Delta Q_j\right) \tag{25}$$

Here, $\partial F_{\text{rad}_i}/\partial Q_j$ denotes the radiative heat flux Jacobian, and is given by

$$\frac{\partial F_{\text{rad}_i}}{\partial Q_j} = \begin{bmatrix} 0 & 0 & 0 \\ 0 & 0 & 0 \\ -\dfrac{\partial q_i}{\partial \rho_j} & -\dfrac{\partial q_i}{\partial \rho u_j} & -\dfrac{\partial q_i}{\partial e_j} \end{bmatrix} \tag{26}$$

The Jacobian elements in Eq. (26) are given by a chain rule

$$\frac{\partial q_i}{\partial \rho_j} = -\left(\frac{\partial q_i}{\partial T_j}\right)\left(\frac{\partial e_j}{\partial \rho_j}\right)\left(\frac{\partial e_j}{\partial T_j}\right)^{-1}$$

$$\frac{\partial q_i}{\partial \rho u_j} = -\left(\frac{\partial q_i}{\partial T_j}\right)\left(\frac{\partial e_j}{\partial \rho u_j}\right)\left(\frac{\partial e_j}{\partial T_j}\right)^{-1}$$

$$\frac{\partial q_i}{\partial e_j} = \left(\frac{\partial q_i}{\partial T_j}\right)\left(\frac{\partial e_j}{\partial T_j}\right)^{-1}$$

Derivation of these Jacobian elements is given in Appendix A. Formulation of $\partial q/\partial T$ is given in Appendix B.

Substituting Eqs. (20) and (23) into Eq. (19), the final form of Eq. (19) becomes

$$\left[I + \frac{\Delta t}{\Delta x}(A_{i+1/2} - A_{i-1/2}) - \frac{\Delta t}{\Delta x}\left(\sum_{j=1}^{i_{\max}} \frac{\partial F^{n}_{\text{rad}_{i+1/2}}}{\partial Q_j} - \sum_{j=1}^{i_{\max}} \frac{\partial F^{n}_{\text{rad}_{i-1/2}}}{\partial Q_j}\right)\right] \Delta Q = -\frac{\Delta t}{\Delta x}(F^{n}_{i+1/2} - F^{n}_{i-1/2}) + \frac{\Delta t}{\Delta x}(F^{n}_{\text{rad}_{i+1/2}} - F^{n}_{\text{rad}_{i-1/2}}) \tag{27}$$

The matrix in the left-hand side of Eq. (27) becomes a fully loaded matrix. The system of linear algebraic equations is solved through a direct matrix inversion.

Flowfield

The present method is used to determine the radiating flowfield behind a reflected shock wave in air. The one-dimensional radiating flowfield behind a reflected shock wave is shown schematically in Fig. 1. The calculation is initiated at the moment when the incident shock reaches the end wall. The solution is marched in time by integrating Eq. (27). The calculation is terminated at 1.5×10^{-5} s after the initiation of the reflected shock flow. The grid interval is 0.05 cm and the grid points are 51. The Courant–Friedrichs–Lewy (CFL) number is set to 0.1.

The initial thermodynamic state behind the incident shock wave is determined by solving the Rankine–Hugoniot relations in chemical equilibrium.[18] The calculation is carried out for the case of the incident shock velocity of 7 to 11 km/s.

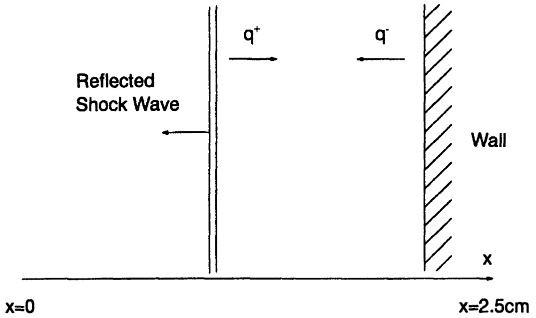

Fig. 1 Schematic of one-dimensional radiating flowfield.

The equilibrium gas properties are calculated by the free energy minimization technique. The results are fed into the program in the form of a table.[19]

The procedure used to obtain the coupled solution is as follows: at first the PRG model is constructed for the initial flowfield to reproduce the multiband calculation. The values of the selection criteria $\Delta\tau_P$ are determined at each cell. The coupling calculation is carried out by computing radiation by the PRG model with the same selection criteria at each time step. The PRG model is updated and the new selection criteria are given at every 25th time step.

An experiment had been performed in the reflected shock region of a 12-in.-diam shock tube.[14] Initially, the shock tube was filled with air to 0.2 torr. The incident shock velocity was varied over the range of 6.5–9.4 km/s. The radiant intensity was measured in the side-view direction, i.e., in the direction normal to the direction of movement of the shock wave. The wavelength-integrated radiation measurement was carried out by using an energy detector.[14] The detector was located inside a large cavity. Radiation was observed through a narrow open windowless slit positioned about 7 mm away from the end wall. When the reflected shock is formed, the gas behind a reflected shock wave leaks through the slit. This leaking gas flow expands toward the cavity gauges. Radiation emerging from the slit is partly absorbed by this expanding gas. The measured radiation intensity was assumed not to be affected by this phenomenon.

The side-view intensity is calculated using a line-by-line technique from the flow solution obtained by the present method. First, the calculation is performed neglecting the existence of the gas leakage through the slit. The emitting medium is a uniform slab in this case, and the space between the slit and the energy detector is a vacuum. The thickness of the uniform slab is 12 cm. Second, the calculation is carried out accounting for the presence of the gas leakage. The cool flow emanating from the slit and moving toward the detector is approximated by two piled layers of uniform property. The thickness of each layer is assumed to be 1 cm. Thermodynamic states of these layers are given as follows: for the first cool layer, $T_{1_{\text{cool}}} = 0.85T_r$ and $P_{1_{\text{cool}}} = 0.55P_r$, where T_r and P_r are the temperature and pressure behind the reflected shock. This condition roughly corresponds to the choking condition of an idealized isentropic expansion. For the second layer, $T_{2_{\text{cool}}}$ and $P_{2_{\text{cool}}}$ are set to $0.39T_{1_{\text{cool}}}$ and $0.03P_{1_{\text{cool}}}$, respectively. This condition is determined arbitrarily to represent the downstream region. The total thickness of these layers is therefore 14 cm. To compare the calculated side-view intensities with experiments, they are scaled by dividing the exponent 0.6 of the thickness of the layer.[14]

In the present calculation, the boundary-layer effect is neglected. Because the radiant intensity was measured 7 mm away from the end wall, as mentioned earlier, the measured radiation is believed to be unaffected by the boundary layer at the end wall.[14]

Results and Discussion

In the present calculations, the typical CPU time for one iteration requires 0.17 s on SX-4 at the National Aerospace

Laboratory. The code runs approximately at 112 Mflops. The computing time for the PRG calculation requires up to 50% of the total CPU time. It is believed that this computing time is shorter at least by a factor of 10 when compared with the time expended in Ref. 11.

Figure 2 shows the variation of the normalized difference in q^+ values between the multiband model and the PRG model at the wall. This figure shows that the PRG model predicts values that agree with the wall radiative heat flux values of the multiband model through the entire calculation. Relatively large error is seen at the beginning of the calculation. However, the wall radiative heat flux value at this time is negligibly small.

Figures 3 and 4 compare the spatial distribution of q and the divergence of radiative heat flux dq/dx between the PRG model and the multiband model for the case of an incident shock velocity of 11 km/s. The elapsed time from the beginning of the coupling calculation is denoted by t. Three cases corresponding to 5×10^{-6}, 1×10^{-5}, and 1.5×10^{-5} s are shown. One can see that the present iteration scheme does not accurately reproduce the radiative heat flux value of the multiband model in the immediately upstream region of the reflected shock wave. Except for this narrow region, good agreements between the multiband model and the PRG model are seen for both the radiative heat flux and the divergence of radiative heat flux.

The convergence histories of the residuals are given in Fig. 5 for the case of the incident shock velocity of 11 km/s. The coupled and uncoupled calculations are shown. The uncoupled calculation is obtained through the conventional inviscid calculation assuming thermochemical equilibrium. The radiation coupling does not affect the convergence histories when compared with the uncoupled calculation. Significant oscillations are caused by the unsteady shock propagation. The variations of other conditions are similar to that of the case presented here and, hence, omitted.

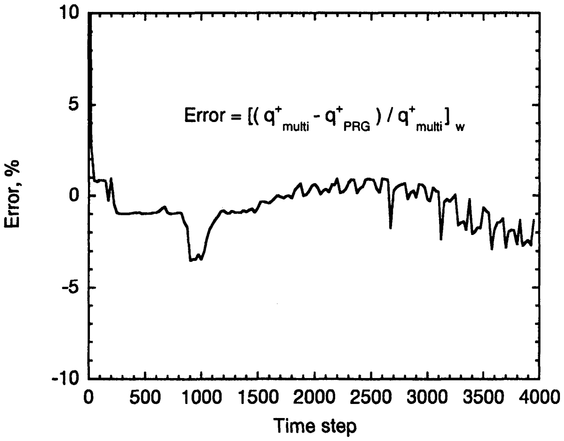

Fig. 2 Variation in the difference in q^+ at the wall between the PRG model and the multiband model for the incident shock velocity 11 km/s.

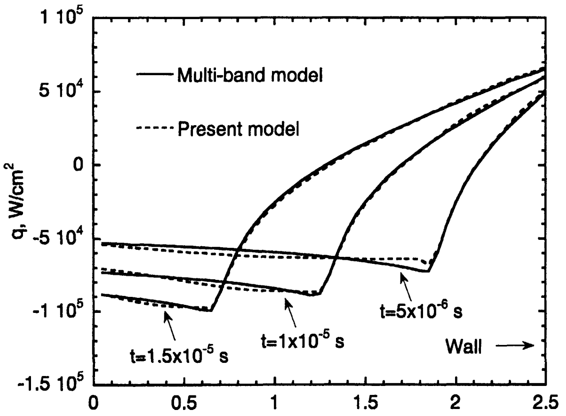

Fig. 3 Comparison of the distribution of the radiative heat flux between the PRG model and the multiband model for the incident shock velocity 11 km/s.

Figures 6 and 7 show the temperature and pressure distributions for the case of the incident shock velocity of 7 km/s. As can be seen from these figures, radiation does not change the flowfield very much at this shock velocity. This result is consistent with the experimental evidence. Figures 8 and 9 show the temperature and pressure distributions for the case of the incident shock velocity of 11 km/s. From these figures, the coupling effect is clearly seen not only in temperature distribution but also in pressure distribution, though the latter is less significant. Some of the emitted radiation is absorbed in the upstream region of the reflected shock wave, i.e., left side of the shock. This is known as the precursor heating phenomenon. The difference in the shock thickness, i.e., the distance between the shock wave and the wall, can also be clearly seen. This is analogous to what is observed in the difference in the shock-layer thickness for a blunt-body calculation between the cases with and without radiative cooling. For a grid convergence check, the temperature distributions using 201 grid points are also shown in Fig. 8. Although a slight difference can be seen particularly near the wall, the overall features are almost the same. Because the radiative intensity is compared at the position of 7 mm away from the end wall, and this position is well outside the region where temperature difference is seen, we regard the accuracy of the calculated results with 51 grid points is sufficient.

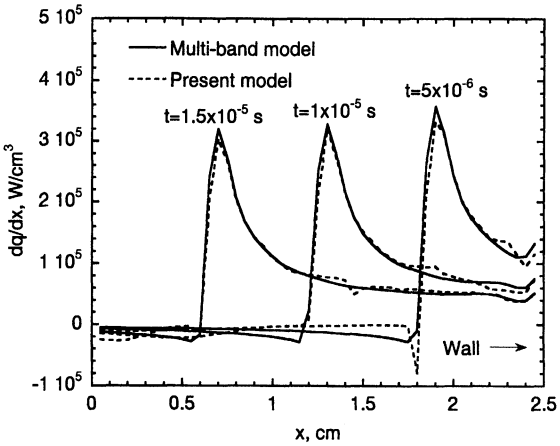

Fig. 4 Comparison of the distribution of the divergence of the radiative heat flux between the PRG model and the multiband model for the incident shock velocity 11 km/s.

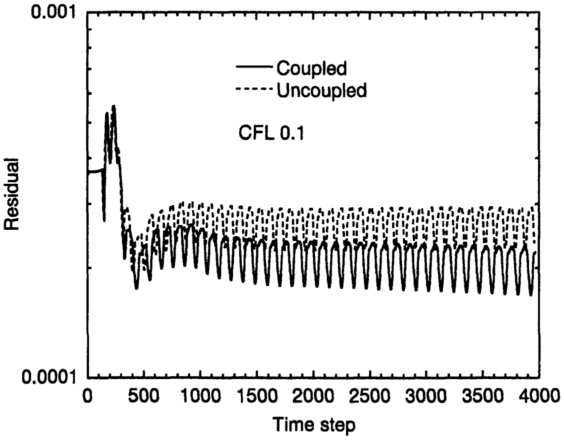

Fig. 5 Variation of the residual for the incident shock velocity 11 km/s.

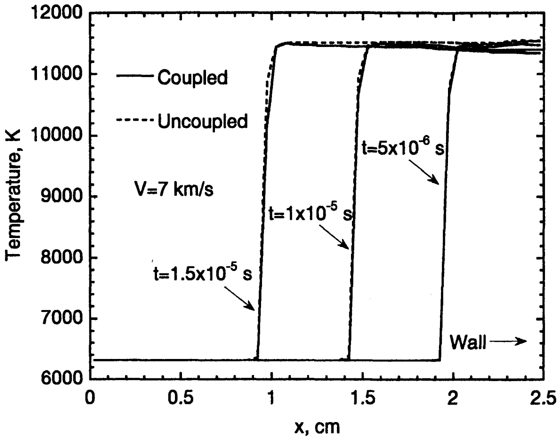

Fig. 6 Comparison of the temperature distribution between the coupled and uncoupled calculation for the incident shock velocity 7 km/s.

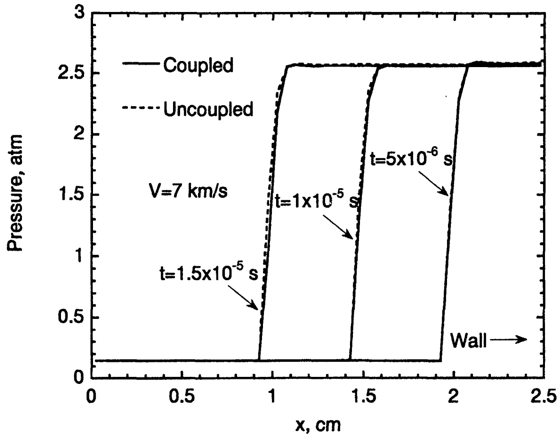

Fig. 7 Comparison of the pressure distribution between the coupled and uncoupled calculation for the incident shock velocity 7 km/s.

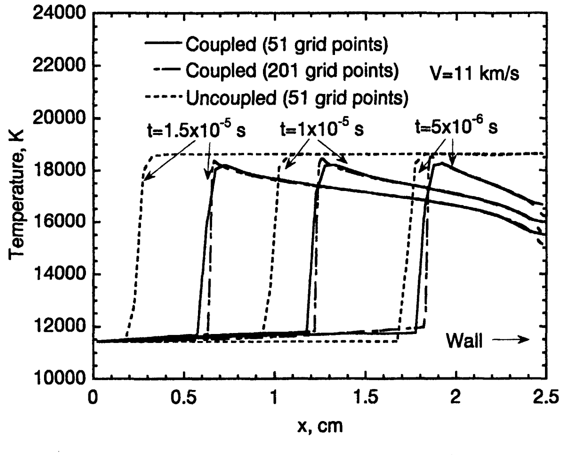

Fig. 8 Comparison of the temperature distribution between the coupled and uncoupled calculation for the incident shock velocity 11 km/s.

The enthalpy values evaluated at the point of 7 mm from the end wall at 1.5×10^{-5} s for both the coupled and uncoupled calculation, and also the equivalent flight velocity, are presented in Fig. 10. These enthalpy values correspond to the equivalent flight velocities in the range of about 10–16 km/s at an altitude of 43 km. The calculations for the high-pressure range are also carried out for demonstrating the robustness of the present method, even though they are not realistic entry conditions.

In Fig. 11, comparison of the radiant intensity between the present calculations and the experiment by Wood et al.[14] is made. In this case, the possible effect of expanding flow at the slit is not considered. From the figure, one can see that the radiative cooling effect is stronger for the higher shock velocity, as expected. However, the coupled calculation slightly overpredicts the experimental data.

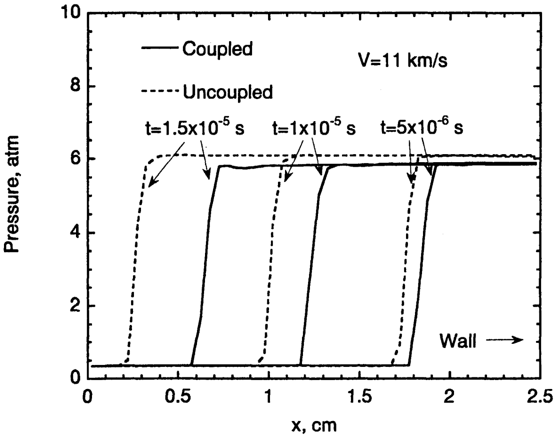

Fig. 9 Comparison of the pressure distribution between the coupled and uncoupled calculation for the incident shock velocity 11 km/s.

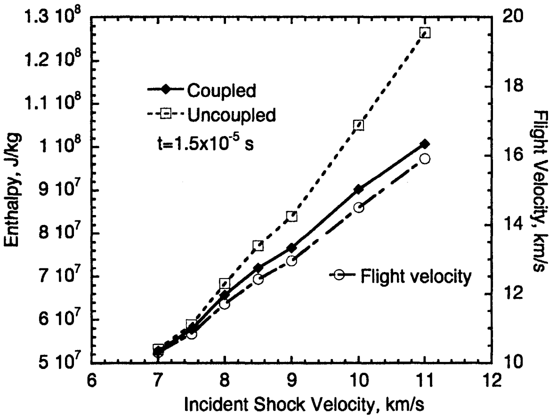

Fig. 10 Comparison of the enthalpy between the coupled and uncoupled calculation. Equivalent flight velocities corresponding to the calculated incident shock velocities are also plotted.

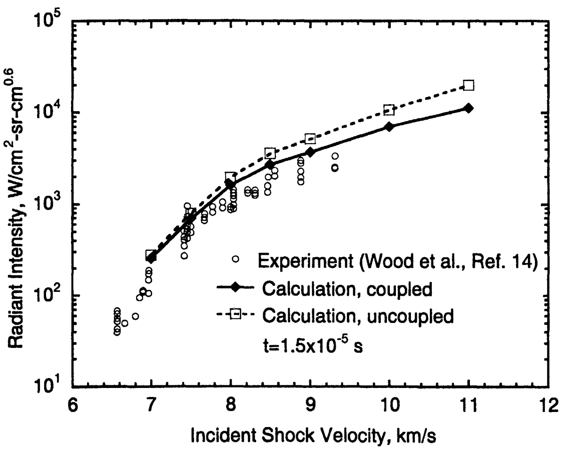

Fig. 11 Comparison of the radiant intensity between the experiments and calculations without the cooling effect of the expanding flow at the slit.

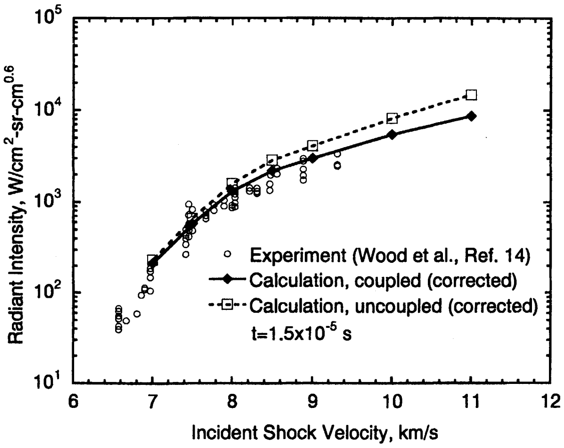

Fig. 12 Comparison of the radiant intensity between the experiments and calculations with the cooling effect of the expanding flow at the slit.

To explain the discrepancy between the present coupled calculation and experiment, the possible cooling effect by the expanding flow at the slit is included. Figure 12 shows the comparison of the radiant intensity between the present calculation accounting for the cooling effect and the experiment. As can be seen, a fair agreement is obtained between the coupled calculation and the experiment, whereas the uncoupled calculation still overestimates the experimental values. This implies that the discrepancy seen in Fig. 11 is a result of the absorption in the expanding flow.

Concluding Remarks

A numerical method for calculating one-dimensional radiating flowfields is developed using the PRG model. The radiative heat fluxes are calculated through the use of the PRG model, and the equations for fluid flows are solved in a fully coupled manner using the full matrix inversion. The present method is successfully applied to a one-dimensional radiating flowfield behind a reflected shock wave where the flow enthalpies correspond to flight velocities up to 16 km/s. A good agreement is seen between the calculation and the available experimental data measured in a shock tube. A high computational efficiency is also attained.

Appendix A: Derivation of Jacobian Elements

Radiative heat flux at ith point, q_i, is a function of ρ, ρu, and e at all points in the flowfield, i.e.,

$$\begin{aligned} q_i = q(&\rho_1, \ldots, \rho_j, \ldots, \rho_i, \ldots, \rho_{i_{\max}}, \\ &\rho u_1, \ldots, \rho u_j, \ldots, \rho u_i, \ldots, \rho u_{i_{\max}}, \\ &e_1, \ldots, e_j, \ldots, e_i, \ldots, e_{i_{\max}}) \end{aligned} \tag{A1}$$

By differentiating Eq. (28) by the jth component, one obtains

$$\mathrm{d}q_i = \left(\frac{\partial q_i}{\partial \rho_j}\right)_{\rho u, e} \mathrm{d}\rho_j + \left(\frac{\partial q_i}{\partial \rho u_j}\right)_{\rho, e} \mathrm{d}\rho u_j + \left(\frac{\partial q_i}{\partial e_j}\right)_{\rho, \rho u} \mathrm{d}e_j \tag{A2}$$

Total energy at jth point, e_j, is given by

$$e_j = \tilde{\varepsilon}_j + \frac{1}{2}\frac{(\rho u_j)^2}{\rho_j} \tag{A3}$$

Because $\tilde{\varepsilon}_j = \tilde{\varepsilon}(\rho_j, T_j)$, the total energy is therefore written as $e_j = e(\rho_j, \rho u_j, T_j)$. Then one obtains

$$\mathrm{d}e_j = \left(\frac{\partial e_j}{\partial \rho_j}\right)_{\rho u, T} \mathrm{d}\rho_j + \left(\frac{\partial e_j}{\partial \rho u_j}\right)_{\rho, T} \mathrm{d}\rho u_j + \left(\frac{\partial e_j}{\partial T_j}\right)_{\rho, \rho u} \mathrm{d}T_j \tag{A4}$$

Substituting Eq. (A4) into Eq. (A1),

$$\begin{aligned} \mathrm{d}q_i = &\left[\left(\frac{\partial q_i}{\partial \rho_j}\right)_{\rho u, e} + \left(\frac{\partial q_i}{\partial e_j}\right)_{\rho, \rho u}\left(\frac{\partial e_j}{\partial \rho_j}\right)_{\rho u, T}\right] \mathrm{d}\rho_j \\ &+ \left[\left(\frac{\partial q_i}{\partial \rho u_j}\right)_{\rho, e} + \left(\frac{\partial q_i}{\partial e_j}\right)_{\rho, \rho u}\left(\frac{\partial e_j}{\partial \rho u_j}\right)_{\rho, T}\right] \mathrm{d}\rho_j \\ &+ \left(\frac{\partial q_i}{\partial e_j}\right)_{\rho, \rho u}\left(\frac{\partial e_j}{\partial T_j}\right)_{\rho, \rho u} \mathrm{d}T_j \end{aligned} \tag{A5}$$

For the purpose of simplicity, the subscripts i and j are omitted hereafter. When ρ and ρu are constant

$$\left(\frac{\partial q}{\partial e}\right)_{\rho, \rho u} = \left(\frac{\partial q}{\partial T}\right)_{\rho, \rho u}\left(\frac{\partial e}{\partial T}\right)_{\rho, \rho u}^{-1} \tag{A6}$$

When ρu and T are constant, and assuming $\mathrm{d}q = 0$, we have

$$\begin{aligned} \left(\frac{\partial q}{\partial \rho}\right)_{\rho u, e} &= -\left(\frac{\partial q}{\partial e}\right)_{\rho, \rho u}\left(\frac{\partial e}{\partial \rho}\right)_{\rho u, T} \\ &= -\left(\frac{\partial q}{\partial T}\right)_{\rho, \rho u}\left(\frac{\partial e}{\partial \rho}\right)_{\rho u, T}\left(\frac{\partial e}{\partial T}\right)_{\rho, \rho u}^{-1} \end{aligned} \tag{A7}$$

Here, the temperature dependence of the radiative heat flux is assumed to be much stronger than the pressure dependence. When ρ and T are constant and assuming $\mathrm{d}q = 0$, we have

$$\begin{aligned} \left(\frac{\partial q}{\partial \rho u}\right)_{\rho, e} &= -\left(\frac{\partial q}{\partial e}\right)_{\rho, \rho u}\left(\frac{\partial e}{\partial \rho u}\right)_{\rho, T} \\ &= -\left(\frac{\partial q}{\partial T}\right)_{\rho, \rho u}\left(\frac{\partial e}{\partial \rho u}\right)_{\rho, T}\left(\frac{\partial e}{\partial T}\right)_{\rho, \rho u}^{-1} \end{aligned} \tag{A8}$$

The derivatives of e with respect to ρ, ρu, and T in Eqs. (A6–A8) are given as follows:

$$\left(\frac{\partial e}{\partial \rho}\right)_{\rho u, T} = \left(\frac{\partial \tilde{\varepsilon}}{\partial \rho}\right)_{\rho u, T} - \frac{1}{2}u^2 \tag{A9}$$

$$\left(\frac{\partial e}{\partial \rho u}\right)_{\rho, T} = u \tag{A10}$$

$$\left(\frac{\partial e}{\partial T}\right)_{\rho, \rho u} = \left(\frac{\partial \tilde{\varepsilon}}{\partial T}\right)_{\rho, \rho u} \tag{A11}$$

The values of $\partial\tilde{\varepsilon}/\partial\rho$ and $\partial\tilde{\varepsilon}/\partial T$ are determined by numerical differentiation.

Appendix B: Formulation of $\partial q/\partial T$

By differentiating Eqs. (10–15) with respect to temperature T, one obtains the following formula for the diagonal elements:

$$\frac{\partial q^+_{P_j}}{\partial T_j} = 2\pi\left(\frac{\partial \kappa_{P_j}}{\partial T_j} B_{P_j}\frac{\Delta x_j}{2} + \kappa_{P_j}\frac{\mathrm{d}B_{P_j}}{\mathrm{d}T_j}\frac{\Delta x_j}{2}\right) \tag{B1}$$

$$\frac{\partial q^-_{P_j}}{\partial T_j} = -2\pi\left(\frac{\partial \kappa_{P_j}}{\partial T_j} B_{P_j}\frac{\Delta x_j}{2} + \kappa_{P_j}\frac{\mathrm{d}B_{P_j}}{\mathrm{d}T_j}\frac{\Delta x_j}{2}\right) \tag{B2}$$

$$\begin{aligned} \frac{\partial q^+_{R_j}}{\partial T_j} = &\ \pi\frac{\mathrm{d}B_{R_j}}{\mathrm{d}T_j} + \frac{2}{3}\pi\frac{1}{\kappa_{R_j}^2}\frac{\partial \kappa_{R_j}}{\partial T_j}\frac{\mathrm{d}B_{R_j}}{\mathrm{d}T_j}\left(\frac{\mathrm{d}T}{\mathrm{d}x}\right)_j \\ &- \frac{2}{3}\pi\frac{1}{\kappa_{R_j}}\frac{\mathrm{d}^2B_{R_j}}{\mathrm{d}T_j^2}\left(\frac{\mathrm{d}T}{\mathrm{d}x}\right)_j \end{aligned} \tag{B3}$$

$$\begin{aligned}\frac{\partial q^{-}_{R_j}}{\partial T_j} &= -\pi \frac{\mathrm{d}B_{R_j}}{\mathrm{d}T_j} + \frac{2}{3}\,\pi \frac{1}{\kappa^2_{R_j}} \frac{\partial \kappa_{R_j}}{\partial T_j} \frac{\mathrm{d}B_{R_j}}{\mathrm{d}T_j} \left(\frac{\mathrm{d}T}{\mathrm{d}x}\right)_j \\ &\quad - \frac{2}{3}\,\pi \frac{1}{\kappa_{R_j}} \frac{\mathrm{d}^2 B_{R_j}}{\mathrm{d}T_j^2} \left(\frac{\mathrm{d}T}{\mathrm{d}x}\right)_j\end{aligned} \tag{B4}$$

$$\begin{aligned}\frac{\partial q^{+}_{G_j}}{\partial T_j} &= 2\pi \Bigg[-\kappa_{G_1} B_{G_1} E_1(j,\,1) \frac{\partial \kappa_{G_j}}{\partial T_j} \frac{\Delta x_j}{2}\,\Delta x_1 \\ &\quad - \kappa_{G_2} B_{G_2} E_1(j,\,2) \frac{\partial \kappa_{G_j}}{\partial T_j} \frac{\Delta x_j}{2}\,\Delta x_2 - \cdots \\ &\quad + \frac{\partial \kappa_{G_j}}{\partial T_j} B_{G_j} E_2(j,j) \frac{\Delta x_j}{2} + \kappa_{G_j} \frac{\mathrm{d}B_{G_j}}{\mathrm{d}T_j} E_2(j,j) \frac{\Delta x_j}{2} \\ &\quad - I_{0_G} E_2(j,\,1) \frac{\partial \kappa_{G_j}}{\partial T_j} \frac{\Delta x_j}{2} \Bigg]\end{aligned} \tag{B5}$$

$$\begin{aligned}\frac{\partial q^{-}_{G_j}}{\partial T_j} &= -2\pi \Bigg[\frac{\partial \kappa_{G_j}}{\partial T_j} B_{G_j} E_2(j,j) \frac{\Delta x_j}{2} + \kappa_{G_j} \frac{\mathrm{d}B_{G_j}}{\mathrm{d}T_j} E_2(j,j) \frac{\Delta x_j}{2} \\ &\quad - \kappa_{G_{j+1}} B_{G_{j+1}} E_1(j+1,j) \frac{\partial \kappa_{G_j}}{\partial T_j} \frac{\Delta x_j}{2}\,\Delta x_{j+1} - \cdots \\ &\quad - \kappa_{G_{j_{\max}}} B_{G_{j_{\max}}} E_1(j_{\max},j) \frac{\partial \kappa_{G_j}}{\partial T_j} \frac{\Delta x_j}{2}\,\Delta x_{j_{\max}} \\ &\quad - I_{w_G} E_2(j_{\max},j) \frac{\partial \kappa_{G_j}}{\partial T_j} \frac{\Delta x_j}{2} \Bigg]\end{aligned} \tag{B6}$$

For the off-diagonal elements

$$\frac{\partial q^{+}_{P_j}}{\partial T_{j'}} = 2\pi \left(\frac{\partial \kappa_{P_{j'}}}{\partial T_{j'}} B_{P_{j'}} \Delta x_{j'} + \kappa_{P_{j'}} \frac{\mathrm{d}B_{P_{j'}}}{\partial T_{j'}} \Delta x_{j'} \right) \tag{B7}$$

$$\frac{\partial q^{-}_{P_j}}{\partial T_{j'}} = -2\pi \left(\frac{\partial \kappa_{P_{j'}}}{\partial T_{j'}} B_{P_{j'}} \Delta x_{j'} + \kappa_{P_{j'}} \frac{\mathrm{d}B_{P_{j'}}}{\partial T_{j'}} \Delta x_{j'} \right) \tag{B8}$$

$$\frac{\partial q^{+}_{R_j}}{\partial T_{j'}} = 0 \tag{B9}$$

$$\frac{\partial q^{-}_{R_j}}{\partial T_{j'}} = 0 \tag{B10}$$

$$\begin{aligned}\frac{\partial q^{+}_{G_j}}{\partial T_{j'}} &= 2\pi \Bigg[-\kappa_{G_1} B_{G_1} E_1(j,\,1) \frac{\partial \kappa_{G_{j'}}}{\partial T_{j'}} \Delta x_{j'} \Delta x_1 \\ &\quad - \kappa_{G_2} B_{G_2} E_1(j,\,2) \frac{\partial \kappa_{G_{j'}}}{\partial T_{j'}} \Delta x_{j'} \Delta x_2 - \cdots \\ &\quad + \frac{\partial \kappa_{G_{j'}}}{\partial T_{j'}} B_{G_{j'}} E_2(j,j') \Delta x_{j'} + \kappa_{G_{j'}} \frac{\mathrm{d}B_{G_{j'}}}{\mathrm{d}T_{j'}} E_2(j,j') \Delta x_{j'} \\ &\quad - \kappa_{G_{j'}} B_{G_{j'}} E_1(j,j') \frac{\partial \kappa_{G_{j'}}}{\partial T_{j'}} \frac{\Delta x_{j'}}{2}\,\Delta x_{j'} \\ &\quad - I_{0_G} E_2(j,\,1) \frac{\partial \kappa_{G_{j'}}}{\partial T_{j'}} \Delta x_{j'} \Bigg]\end{aligned} \tag{B11}$$

$$\begin{aligned}\frac{\partial q^{-}_{G_j}}{\partial T_{j'}} &= -2\pi \Bigg[\frac{\partial \kappa_{G_{j'}}}{\partial T_{j'}} B_{G_{j'}} E_2(j',j) \Delta x_{j'} \\ &\quad + \kappa_{G_{j'}} \frac{\mathrm{d}B_{G_{j'}}}{\mathrm{d}T_{j'}} E_2(j',j) \Delta x_{j'} \\ &\quad - \kappa_{G_{j'}} B_{G_{j'}} E_1(j',j) \frac{\partial \kappa_{G_{j'}}}{\partial T_{j'}} \frac{\Delta x_{j'}}{2}\,\Delta x_{j'} \\ &\quad - \kappa_{G_{j'+1}} B_{G_{j'+1}} E_1(j'+1,j) \frac{\partial \kappa_{G_{j'}}}{\partial T_{j'}} \Delta x_{j'} \Delta x_{j'+1} - \cdots \\ &\quad - \kappa_{G_{j_{\max}}} B_{G_{j_{\max}}} E_1(j_{\max},j) \frac{\partial \kappa_{G_{j'}}}{\partial T_{j'}} \Delta x_{j'} \Delta x_{j_{\max}} \\ &\quad - I_{w_G} E_2(j_{\max},j) \frac{\partial \kappa_{G_{j'}}}{\partial T_{j'}} \Delta x_{j'} \Bigg]\end{aligned} \tag{B12}$$

The differentiation of the three mean absorption coefficients with respect to temperature are included in the $\partial q/\partial T$. These are determined by using Eq. (16) and are presented for the table values.

References

[1] Cornette, E. S.,"Forebody Temperatures and Calorimeter Heating Rates Measured During Project Fire II Reentry at 11.35 Kilometers per Second," NASA TM X-1305, Nov. 1966.

[2] Pitts, W. C., and Wakefield, R. M., "Performance of Entry Heat Shields on Pioneer Venus Probes," *Journal of Geophysical Research*, Vol. 85, No. A13, 1980, pp. 8333–8337.

[3] Milos, F. S.,"Galileo Probe Heat Shield Ablation Experiment," AIAA Paper 96-1823, June 1996.

[4] Park, C., "Nonequilibrium Air Radiation (NEQAIR) Program: User's Manual," NASA TM-86707, July 1985.

[5] Park, C., and Milos, F. S., "Computational Equations for Radiating and Ablating Shock Layers," AIAA Paper 90-0356, Jan. 1990.

[6] Hartung, L. C., "Development of a Nonequilibrium Radiative Prediction Method for Coupled Flowfield Solutions," *Journal of Thermophysics and Heat Transfer*, Vol. 6, No. 4, 1992, pp. 618–625.

[7] Hartung, L. C., Micheltree, R. A., and Gnoffo, P. A., "Coupled Radiation Effects in Thermochemical Nonequilibrium Shock Capturing Flowfield Calculation," AIAA Paper 92-2868, July 1992.

[8] Olynick, D. R., Henline, W. D., Chamber, L. H., and Candler, G. V., "Comparisons of Coupled Radiative Flow Solutions with Project Fire II Flight Data," *Journal of Thermophysics and Heat Transfer*, Vol. 9, No. 4, 1995, pp. 586–594.

[9] Gökçen, T., "Computation of Nonequilibrium Radiating Shock Layers," *Journal of Thermophysics and Heat Transfer*, Vol. 9, No. 1, 1995, pp. 34–40.

[10] Nicolet, W. E., Waterland, L. R., and Kendall, R. M., *Methods for Predicting Radiation-Coupled Flowfields About Planetary Entry Probes*, edited by L. S. Fletcher, Vol. 59, Progress in Astronautics and Aeronautics, AIAA, New York, 1978, pp. 120–136.

[11] Gökçen, T., and Park, C., "The Coupling of Radiative Transfer to Quasi 1-D Flows with Thermochemical Nonequilibrium," AIAA Paper 91-0570, Jan. 1991.

[12] Gally, T. A., and Carlson, L. A., "Nonequilibrium Chemical and Radiation Coupling, Part II: Results for AOTV Flowfields," *Journal of Thermophysics and Heat Transfer*, Vol. 6, No. 3, 1992, pp 392–399.

[13] Sakai, T., Sawada, K., and Park, C., "Assessment of Planck-Rosseland-Gray Model for Radiating Shock Layer," AIAA Paper 97-2560, June 1997.

[14] Wood, A. D., Hoshizaki, H., Andrews, J. C., and Wilson, K. H., "Measurements of the Total Radiant Intensity of Air," *AIAA Journal*, Vol. 7, No. 1, 1969, pp. 130–139.

[15] Vincenti, W. G., and Kruger, C. H., *Introduction to Physical Gas Dynamics*, Wiley, New York, 1965.

[16] Abramowitz, M., and Stegum, I. A., "Handbook of Mathematical Functions," *National Bureau of Standards Applied Mathematics Series 55*, Washington, DC, 1964, pp. 227–251.

[17] Steger, J. L., and Warming, R. F., "Flux Vector Splitting of the Inviscid Gasdynamic Equations with Application to Finite-Difference Methods," *Journal of Computational Physics*, Vol. 40, No. 2, 1981, pp. 263–293.

[18] Gordon, S., and McBride, B. J., "Computer Program for Calculation of Complex Chemical Equilibrium Compositions, Rocket Performance, Incident and Reflected Shocks and Chapman-Jouguet Detonations," NASA SP-273, Feb. 1971.

[19] Sawada K., and Dendou, E. "Validation of Hypersonic Equilibrium Flow Calculations Using Ballistic-Range Data," AIAA Paper 97-0344, Jan. 1997.